PAPER

Analytic treatment of nonparaxial full-Poincaré fields: singularity structure and trapping properties

To cite this article: Rodrigo Gutiérrez–Cuevas and Miguel A Alonso 2021 *J. Opt.* **23** 024005

View the article online for updates and enhancements.

Analytic treatment of nonparaxial full-Poincaré fields: singularity structure and trapping properties

Rodrigo Gutiérrez–Cuevas[1,*] **and Miguel A Alonso**[1,2,3]

[1] Aix Marseille Univ, CNRS, Centrale Marseille, Institut Fresnel, UMR 7249, 13397 Marseille Cedex 20, France
[2] The Institute of Optics, University of Rochester, Rochester, NY 14627, United States of America
[3] Center for Coherence and Quantum Optics, University of Rochester, Rochester, NY 14627, United States of America

E-mail: rodrigo.gutierrez-cuevas@fresnel.fr and miguel.alonso@fresnel.fr

Abstract
An analytic extension to the nonparaxial regime of the full-Poincaré (FP) beams is presented. Instead of the stereographic mapping used in the paraxial case, these FP fields are defined in terms of a mapping from the polarization Poincaré sphere onto the sphere of plane-wave directions. It is shown that multipolar fields with complex arguments can be used to implement this mapping and provide closed-form expressions. The three-dimensional polarization singularities of the resulting fields are studied with the help of auxiliary fields presenting vortices at points where the polarization is circular or linear. Finally, the Mie scattering and trapping properties of the FP fields are studied, both of which are greatly simplified by the choice of fields.

Keywords: full-Poincaré fields, polarization singularities, structured light, Mie scattering

(Some figures may appear in colour only in the online journal)

1. Introduction

The study of structured light has seen significant growth in the last decades, leading to applications in numerous fields such as imaging, information transfer, and micromanipulation [1–3]. This is in large part due to the development of efficient and accessible methods for structuring light, such as the generation of phase singularities through diffraction holograms as proposed by Soskin and collaborators [4–6]. These methods have since evolved, and now allow shaping all of light's degrees of freedom [7–10], including polarization [3, 11]. For example, the use of radially and azimuthally polarized light has expanded the control of optical traps [12] and the generally nonseparable nature of modal and polarization structure of light has proven useful for quantum information applications [13, 14].

Just like scalar fields can present phase singularities, nonuniformly polarized vector beams generally possess polarization singularities [15–19]. These structurally-stable features come in two types: C points, which are points of circular polarization where the direction of the major axis is ill-defined, and L points, which are points of linear polarization where handedness is ill-defined. Particular emphasis has been placed on the study of C points, since they trace lines in three-dimensional space, which can form closed loops and knots, even in the paraxial regime [20–24]. C points can be further classified according to the distribution of the polarization lines traced by the major axes of the surrounding polarization ellipses. There are three main types of C points: 'lemon', 'star', and 'monstar', where one, three, and an infinite number of polarization lines terminate, respectively. These types of C points are the ones that appear 'in the wild', i.e. in random fields [16, 17, 21]. However, higher-order singularities can be generated with purposefully designed fields [19, 25–27]. Note

* Author to whom any correspondence should be addressed.

that for the very restrictive case of purely linearly-polarized fields there is a third type of polarization singularity, V points [25], where the direction of linear polarization is not defined, e.g. at the axis of radially and azimuthally polarized fields. In this work we consider the more common case of fields in which the polarization ellipticity changes in space.

Full-Poincaré (FP) beams are examples of vector beams with nonuniform polarization distributions, which were introduced as a way to map all possible paraxial polarization states onto each transverse plane of a beam [28–30]. They can be expressed as the superposition of orthogonaly-polarized Gaussian and vortex Laguerre-Gauss beams. At the waist plane this superposition can be written as
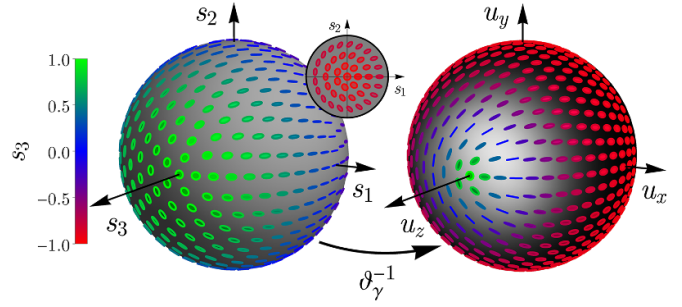
$$\mathbf{E} = E_0 \left(\cos\alpha\, \mathbf{v}_1 + \sin\alpha \frac{\rho}{w} e^{i\phi}\, \mathbf{v}_2 \right) e^{-\rho^2/w^2}, \qquad (1)$$

where $\mathbf{v}_1^{\dagger} \cdot \mathbf{v}_2 = 0$, $\|\mathbf{v}_1\| = \|\mathbf{v}_2\| = 1$, w is the waist of the Gaussian, α is the mixing angle controlling the ratio between the two polarization components, E_0 is a global amplitude factor, and ρ and ϕ are the polar coordinates. Fully polarized paraxial light is commonly described with the help of a Jones vector,

$$\mathbf{v}(\vartheta, \varphi) = \cos\frac{\vartheta}{2} e^{-i\varphi/2} \boldsymbol{\epsilon}_+ + \sin\frac{\vartheta}{2} e^{i\varphi/2} \boldsymbol{\epsilon}_-, \qquad (2)$$

written here in terms of the circular polarization vectors $\boldsymbol{\epsilon}_\pm = (\hat{\mathbf{x}} \pm i\hat{\mathbf{y}})/2^{1/2}$. The angles ϑ and φ are the polar and azimuthal coordinates on the Poincaré sphere (PS) as shown in figure 1. Comparing equations (1) and (2), it can be seen that, geometrically, the polarization distribution of a FP beam is given by a stereographic projection of the PS onto the transverse plane mapping the polarization $\mathbf{v}_1$ to the origin and $\mathbf{v}_2$ to infinity. In particular, if $\mathbf{v}_1$ and $\mathbf{v}_2$ are chosen to be left- and right-circular polarization vectors, the resulting FP beam exhibits either a lemon or star C point polarization singularity at the origin. For a FP beam of the type in equation (1) the mapping is one-to-one; however, by changing the vortex charge and/or considering higher-order radial modes, the PS can be mapped several times onto to transverse plane. These higher-order FP beams can also lead to higher-order polarization singularities [25, 26, 30, 60]. Generalizations of FP beams into the nonparaxial regime have been proposed [28, 31, 32, 60], but these are either not given by closed-form expressions or are not defined in terms of a simple geometrical mapping allowing a direct extension to higher-order fields.

Here, it is shown that a geometrical mapping is possible in the nonparaxial regime between the PS and the sphere of directions (SDs). This is achieved by considering superpositions of simple multipoles evaluated at complex arguments [33, 34] leading to closed-form solutions of Maxwell's equations that reduce to LG beams in the paraxial regime [35–38]. It is shown that, for these fields, the transverse polarization distribution (which only takes into account the transverse components of the electric field) mimics that of the paraxial FP beams. Additionally, the full three-dimensional structure is examined with the help of auxiliary complex scalar and vector fields presenting phase vortices at points where the polarization is circular or linear. Lastly, the Mie scattering and trapping properties of the nonparaxial FP fields is studied.

Figure 1. Mapping of the PS (left) onto the SD (right) through the function ϑ_γ^{-1} given in equation (6). The axes of the PS are the normalized Stokes parameters s_j and the inset shows the area around $s_3 = -1$. The amplitude and polarization distribution of the plane-wave spectrum for the lemon FP field with $k\zeta = 5$ and $\delta = \pi/4$, which determine the parameter γ of the mapping, are shown in the SD.

2. Definition of nonparaxial FP fields

2.1. Sphere-to-sphere mapping

An electromagnetic monochromatic field with wavenumber k propagating in free space can be written as a superposition of plane waves,

$$\mathbf{E}(\mathbf{r}) = \int_{4\pi} \mathbf{A}(\mathbf{u}) e^{i k \mathbf{u} \cdot \mathbf{r}} \, d\Omega, \qquad (3)$$

where the unit vector $\mathbf{u} = (\cos\phi \sin\theta, \sin\phi \sin\theta, \cos\theta)$ indicates the direction of propagation of each plane wave, parametrized here in terms of the polar and azimuthal angles θ and ϕ. The plane-wave spectrum $\mathbf{A}(\mathbf{u})$, which is proportional to the far field, is a vector field defined over the SDs for $\mathbf{u}$. The transversality condition implies that $\mathbf{u} \cdot \mathbf{A}(\mathbf{u}) = 0$ so that $\mathbf{A}$ is tangent to the surface of the SD and can be expressed in terms of a polarization basis conformed of a pair of orthogonal vectors $\mathbf{V}_{\mathbf{u}}$ and $\mathbf{u} \times \mathbf{V}_{\mathbf{u}}^{\dagger}$ satisfying $\mathbf{u} \cdot \mathbf{V}_{\mathbf{u}} = 0$. Locally, these vectors span a plane in which we can define a polarization state through the standard paraxial formulas. Therefore, we can generalize FP beams to the nonparaxial regime by means of the more natural mapping from the PS to the SD (see figure 1). This mapping is further motivated by the fact that, in the paraxial regime, only the small cap of the SD in the forward direction is occupied by the plane-wave spectrum, which then coincides with the 2D Fourier transform of the paraxial beam at the waist plane; for paraxial FP beams, this Fourier spectrum exhibits a polarization pattern similar to that in configuration space, so that the stereographic projection of the PS also applies to the plane-wave spectrum.

The implementation of this sphere-to-sphere mapping requires an appropriate polarization basis over the SD. A good option is $\mathbf{V}_{\mathbf{u}}^{(\pm)} = \exp(i\pi/4)(\mathbf{u} \times \boldsymbol{\epsilon}_\pm \times \mathbf{u} \pm i\mathbf{u} \times \boldsymbol{\epsilon}_\pm)$ [37], which maps circular polarization according to parallel transport from the forward $+\hat{\mathbf{z}}$ direction and is therefore consistent with the Richards–Wolf theory of focusing systems [36, 37, 39, 40]. These vectors are not normalized to unity; instead they satisfy $\|\mathbf{V}_{\mathbf{u}}^{(\pm)}\| = \cos(\theta/2)$ and thus vanish as $\mathbf{u}$ approaches $-\hat{\mathbf{z}}$, which is a degenerate singularity of this basis

[36, 37, 41], chosen to be as distant as possible from the $+\hat{\mathbf{z}}$ direction around which the plane-wave spectrum of directional fields concentrates.

These considerations raise, in turn, requirements on the mapping from the PS to the SD. This mapping must mimic the plane-wave spectrum of focused fields and hence allow the concentration of most polarization states within the forward-propagating hemisphere. By rewriting the Jones vector in the following form

$$\mathbf{v}(\vartheta,\varphi) = \frac{e^{-i\varphi/2}}{2\cos\frac{\vartheta}{2}}\left[(1+\cos\vartheta)\boldsymbol{\epsilon}_+ + \sin\vartheta e^{i\varphi}\boldsymbol{\epsilon}_-\right], \quad (4)$$

we can see that one way to concentrate polarization states around the forward direction is to write the plane-wave spectrum for a lemon (+) or a star (−) FP field as

$$\mathbf{A}^{(\pm)}(\theta,\phi) = E_0\left[(1+\cos\theta)\mathbf{V}_{\mathbf{u}}^{(\pm)} + \gamma\sin\theta e^{i\phi}\mathbf{V}_{\mathbf{u}}^{(\mp)}\right]f(\theta), \quad (5)$$
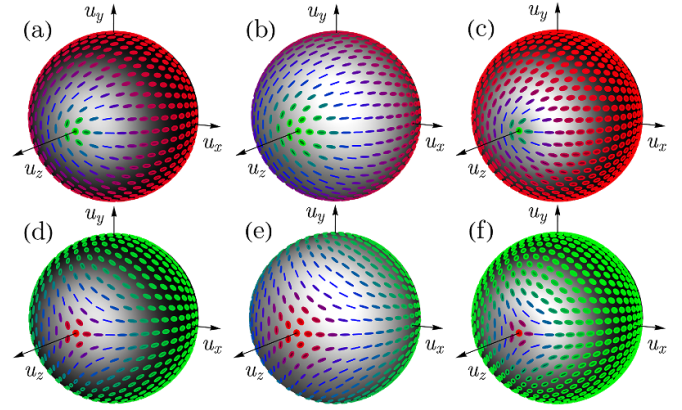
which has the same basic form as the Jones vector in equation (4) but changes the ratio of each polarization by the introduction of the parameter γ. This change of ratio defines the mapping

$$\vartheta_\gamma(\theta) = \frac{\pi}{2} - \tan^{-1}\left(\frac{1}{\gamma}\cot\theta + \frac{1-\gamma^2}{2\gamma}\tan\frac{\theta}{2}\right), \quad (6)$$

between the PS and the SD. For the lemon FP field, when $\gamma > 1$ the circle of linear polarization for $\mathbf{A}$ is moved into the forward-propagating hemisphere while leaving the left-circular polarization fixed at $u_z = -1$, as shown in figure 1 and two lemon C point singularities appear at the poles. For the star FP fields, the locations of right and left circular polarizations are reversed and two star C points appear at the poles. Note that the mapping defined by equations (5) and (6) over the SD is analogous to the one enacted on the PS by a dichroic element [42].

2.2. Plane-wave spectrum

Equation (5) allows concentrating most of the polarization structure into the forward-propagating hemisphere. The same type of concentration is then needed for the amplitudes of the plane waves through the function $f(\theta)$. Many such weight functions could be used but not all would lead to a simple analytic expression in configuration space. One option that provides both an analytic expression for the electric field through equation (3) and a continuous connection to the paraxial regime is $f(\theta) = \exp(k\zeta\cos\theta)$ [43]. This real exponential can be interpreted as an imaginary shift $z \to z - i\zeta$ in configuration space [33, 34]. Assuming a normalized plane wave spectrum according to $\int \|\mathbf{A}\|\, d\Omega = |E_0|^2$, the expression for the lemon and star FP fields in equation (5) can be rewritten as

Figure 2. Effect to the parameters ζ and δ on the plane-wave spectrum and its polarization distribution: for the (a)–(c) lemon and (d)–(f) star FP fields with (a), (d) $k\zeta = 5$ and $\delta = \pi/4$, (b), (e) $k\zeta = 1$ and $\delta = \pi/4$, and (c), (f) $k\zeta = 5$ and $\delta = \pi/3$.

$$\begin{aligned}
\mathbf{A}^{(\pm)}(\mathbf{u}) &= \frac{E_0}{\sqrt{4\pi}}\left[\alpha_r(\zeta)\cos\delta\,(1+\cos\theta)\,\mathbf{V}_{\mathbf{u}}^{(\pm)} \right.\\
&\quad \left. - \alpha_v(\zeta)\sin\delta\sqrt{\frac{3}{2}}\sin\theta e^{i\phi}\,\mathbf{V}_{\mathbf{u}}^{(\mp)}\right]e^{k\zeta\cos\theta}\\
&= E_0\left\{\alpha_r(\zeta)\cos\delta\,\mathbf{V}_{\mathbf{u}}^{(\pm)}\left[Y_{0,0}(\theta,\phi) + \frac{1}{\sqrt{3}}Y_{1,0}(\theta,\phi)\right]\right.\\
&\quad \left. - \alpha_v(\zeta)\sin\delta\,\mathbf{V}_{\mathbf{u}}^{(\mp)}Y_{1,1}(\theta,\phi)\right\}e^{k\zeta\cos\theta}, \quad (7)
\end{aligned}$$

where α_r and α_v are normalization coefficients. In order to give a hint of how these expressions can be generalized to higher orders, the second form is written in terms of the spherical harmonics,

$$Y_{l,m}(\theta,\phi) = \sigma_m^m\sqrt{\frac{(2l+1)(l-m)!}{4\pi(l+m)!}}P_l^{(m)}(\cos\theta)e^{im\phi} \quad (8)$$

where $\sigma_m = \text{sgn}(m+1/2)$ and $P_l^{(m)}$ is the associated Legendre polynomial. (Note that other FP fields can be generated by replacing the two polarization vectors $\mathbf{V}_{\mathbf{u}}^{(\pm)}$ with two orthogonal linear combinations of these vectors.) The parameter γ introduced in equation (6) becomes a function of δ and ζ,

$$\gamma(\delta,\zeta) = \sqrt{\frac{3}{2}}\frac{\alpha_v(\zeta)}{\alpha_r(\zeta)}\tan\delta. \quad (9)$$

The effect of ζ and δ on the amplitude and polarization distribution of $\mathbf{A}$ is shown in figure 2. The directionality parameter ζ, which corresponds to the Rayleigh range in the paraxial limit, has a similar effect on both the amplitude and the polarization distributions: for increasing ζ they become more concentrated around the $+\hat{\mathbf{z}}$ direction, whereas the parameter δ only controls the ratio of the two orthogonal components thus allowing changing the polarization distribution independently from the focusing properties.

In the paraxial limit, i.e. for $k\zeta \gg 1$, the plane-wave spectrum in equation (7) expressed as an exponential weight times the superposition of $Y_{0,0}$ and $Y_{1,1}$ indeed corresponds to the superposition of a Gaussian and the lowest-order Laguerre–Gauss mode with a vortex [as the one in equation (1)]. However, note that the term $Y_{1,0}$ is needed to achieve the one-to-one mapping between the spheres. This term alone tends in the paraxial limit to an LG beam with a higher-order radial structure, which is not present in the original FP beams [see equation (1)] [33, 34, 36, 37]. This extra term is a nonparaxial correction whose relative amplitude vanishes in the paraxial limit. For $k\zeta > 3$, the relative weight of this extra term is less than 5%, hinting that its effect is only significant for considerably focused fields. Therefore, the FP fields defined here do reduce to the standard FP beams in the paraxial limit.

2.3. Configuration space

The advantage of using imaginary shifts in z is the resulting simplicity of the expressions in configuration space, as opposed to the most common approach of using the Richards–Wolf theory which usually requires numerical integration [31, 32, 39, 40]. Using the relation

$$\Lambda_{l,m}(\mathbf{r}) = \int_{4\pi} Y_{l,m}(\mathbf{u})e^{i k \mathbf{u} \cdot \mathbf{r}} d\Omega, \quad (10)$$

satisfied between the spherical harmonics and the scalar multipoles,

$$\Lambda_{l,m}(\mathbf{r}) = 4\pi i^l j_l(kr) Y_{l,m}(\theta_r, \phi_r), \quad (11)$$
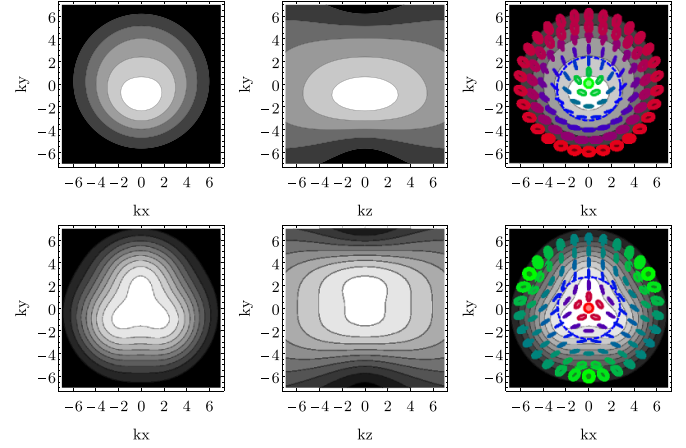
where j_l are the spherical Bessel functions, and the fact that the polarization operators in configuration space are obtained by performing the substitution $\mathbf{u} \to \nabla/ik$, the FP fields in configuration space can be written as

$$\mathbf{E}^{(\pm)}(\mathbf{r};\zeta) = E_0 \Bigg\{ \alpha_r(\zeta)\cos\delta \, \mathbf{V}_\mathbf{r}^{(\pm)} \Big[\Lambda_{0,0}(\mathbf{r} - i\zeta\hat{\mathbf{z}}) \\ + \frac{1}{\sqrt{3}} \Lambda_{1,0}(\mathbf{r} - i\zeta\hat{\mathbf{z}}) \Big] \\ - \alpha_v(\zeta)\sin\delta \, \mathbf{V}_\mathbf{r}^{(\mp)} \Lambda_{1,1}(\mathbf{r} - i\zeta\hat{\mathbf{z}}) \Bigg\}, \quad (12)$$

where

$$\mathbf{V}_\mathbf{r}^{(\pm)} = \frac{1}{k^2}\boldsymbol{\epsilon}_\pm \times \nabla \times \nabla \mp \frac{1}{k}\boldsymbol{\epsilon}_\pm \times \nabla. \quad (13)$$

Note that the derivatives can be computed analytically using the recurrence relations for spherical Bessel functions and associated Legendre polynomials, thus providing a closed-form expression for the fields in configuration space. An implementation of this type of fields can be found in [44]. As shown in figure 3, the amplitude distribution depends on the polarization distribution. For both the lemon and star FP fields the amplitude distribution is no longer circularly symmetric but carries a distinct signature from the polarization distribution in the SD. This coupling between amplitude and polarization has the same origin as the spin–orbit coupling [45].

Figure 3. Amplitude distribution for the lemon (top) and star (bottom) FP fields, with $k\zeta = 5$ and $\delta = \pi/4$, over the x–y plane (left) and the y–z plane (center), and the amplitude over the x–y plane with the transverse polarization distribution overlaid (right), with the dashed blue line corresponding to the L line.

Figure 3 also shows the transverse polarization distribution (which consider only the x and y components of the field) at the focal plane. This distribution resembles that of the paraxial FP beams and the one encoded in the plane-wave spectrum. Nonetheless, focusing causes some small changes such as a slight deformation of the L line in the lemon FP due to the asymmetric shape. It should also be noticed that the polarization pattern at the focal plane is rotated by 45° with respect to the one encoded in the plane-wave spectrum due to the difference in Gouy phase acquired between the two polarization components as they propagate from the focal plane to the far field [28].
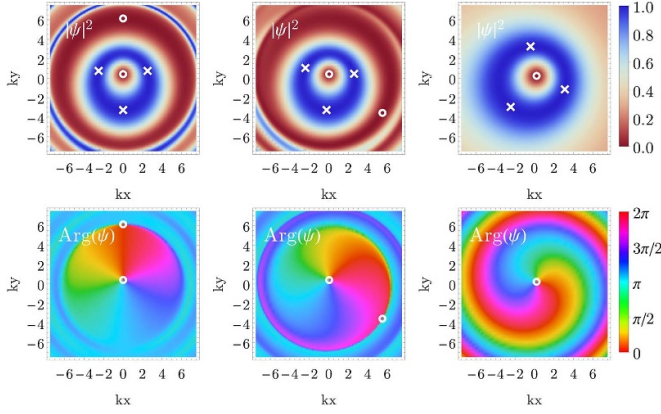
3. True polarization singularities

3.1. Transverse vs true polarization singularities

The transverse polarization of electromagnetic fields exhibits an analogous behavior to the polarization of paraxial fields since it only takes into account two field components. In particular, upon propagation, transverse C singularities trace three-dimensional lines while L singularities are distributed across surfaces. This fact can be understood from the number of constraints required to obtain each type of singularity [15, 16, 18]. C point singularities are formed when the real and imaginary parts of the electric field vector are orthogonal and have equal norm. These two constraints restrict the C singularities to lines in space. L points, on the other hand, are formed when the phase difference between the two components is zero modulo π. This single constraint restrict L points to surfaces in space.

In the nonparaxial regime, the longitudinal component becomes non-negligible and thus must be taken into account for a complete description. This extra component allows the polarization ellipse to have an arbitrary 3D orientation. The true circular and linear polarization singularities, denoted respectively by C^T and L^T, take all three components into account [15, 16, 18]. Both these singularities behave similarly,

Figure 4. Modulus squared (top) and argument (bottom) of ψ for the lemon FP field with $k\zeta = 5$ and $\delta = \pi/4$ at (from left to right) $kz = 0$, 1/2 and 1. The circles and crosses represent, respectively, C^T points (zeros of ψ) and L^T points (maxima where $|\psi| = 1$).

Figure 5. Modulus squared (top) and argument (bottom) of ψ for the star FP field with $k\zeta = 5$ and $\delta = \pi/4$ at (from left to right) $kz = 0$, 1/2 and 1. The circles and crosses represent, respectively, C^T points (zeros of ψ) and L^T points (maxima where $|\psi| = 1$). These plots use the same color palettes as figure 4.

tracing lines across space, due to the number of constraints needed to define them: for a C^T point the real and imaginary parts of the electric field must be orthogonal and of equal norm, as in the transverse case; for L^T points, the phase difference between the three components must vanish modulo π, hence imposing also two constraints.

The dimensionality of transverse (or paraxial) and true polarization singularities can also be understood from the corresponding geometrical representations of polarization. The paraxial or transverse polarization can be represented as a point on the surface of the PS. Circular polarization corresponds to isolated points (the poles), while linear polarization spans a line (the equator). The prescription of three-dimensional polarization requires instead two points on the surface of a unit sphere rather than one [46, 47] and the limiting cases of linear and circular polarization correspond to these two coinciding or being antipodal, respectively, both situations imposing the same number of constraints.

3.2. True C point singularities

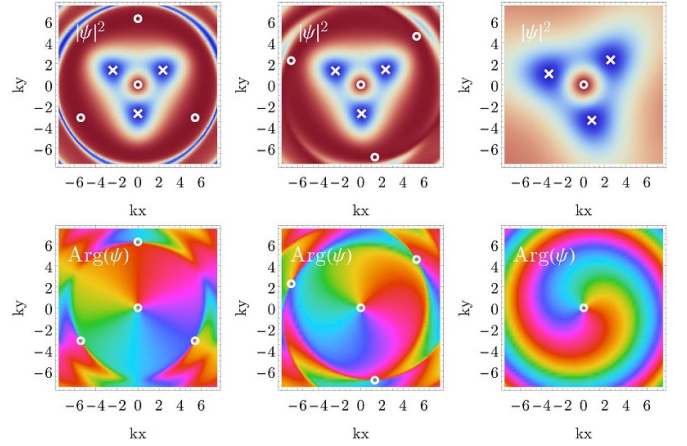The electric spin density vector is defined as

$$\mathbf{S} = \frac{\text{Im}(\mathbf{E}^* \times \mathbf{E})}{||\mathbf{E}||^2}, \tag{14}$$

which points along the normal of the polarization ellipse and whose norm determines the ellipticity. This norm of this vector is unity at C^T points and zero at L^T points. Another relevant quantity is the complex scalar quadratic field

$$\psi = \frac{\mathbf{E} \cdot \mathbf{E}}{||\mathbf{E}||^2}, \tag{15}$$

which vanishes at C^T points where it exhibits phase singularities. The vortices of ψ greatly simplify the identification and tracking of C^T lines across space [16, 22, 48, 49]. These two quantities are related via

$$||\mathbf{S}||^2 = 1 - |\psi|^2. \tag{16}$$

Figures 4 and 5 show the modulus squared and phase of ψ for the lemon and star FP fields, respectively. Both fields have a C^T point near or at the transverse C point (which lies at the origin); for the lemon FP field it is translated slightly along the positive y axis due to the field's asymmetry while for the star FP field it is exactly at the origin. Both fields present other C^T points at regions where the fields become negligible.

3.3. True L point singularities

L^T points correspond to the zeros of the electric spin field, which is real. It is possible to also define a complex vector field whose vortices facilitate tracking the L^T lines:

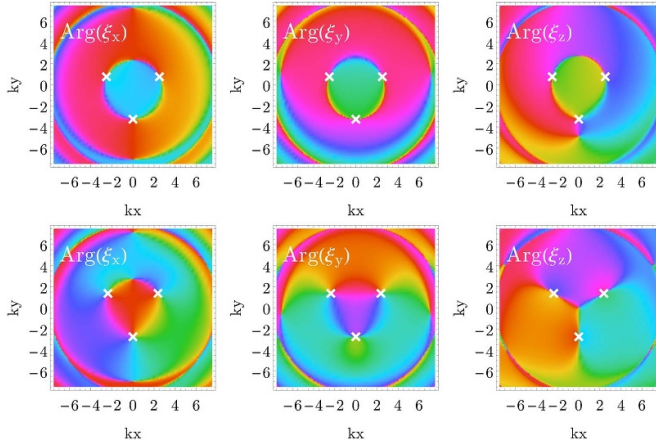$$\boldsymbol{\xi} = \frac{1}{\sqrt{2}}(S_z - iS_y, S_x - iS_z, S_y - iS_x), \tag{17}$$

which vanishes where $\mathbf{S}$ does, since it satisfies $||\boldsymbol{\xi}|| = ||\mathbf{S}||$. The components of this field can be written in terms of the electric field as

$$\xi_x = \frac{\sqrt{2}}{||\mathbf{E}||^2} \left[\text{Im}(E_x^* E_y) + i \, \text{Im}(E_x^* E_z) \right], \tag{18a}$$

$$\xi_y = \frac{\sqrt{2}}{||\mathbf{E}||^2} \left[\text{Im}(E_y^* E_z) + i \, \text{Im}(E_y^* E_x) \right], \tag{18b}$$

$$\xi_z = \frac{\sqrt{2}}{||\mathbf{E}||^2} \left[\text{Im}(E_z^* E_x) + i \, \text{Im}(E_z^* E_y) \right]. \tag{18c}$$

This definition is analogous to the one used to introduce the Stokes fields given by complex combinations of the Stokes parameters providing a simple way to identify polarization singularities in paraxial fields [27, 50, 51]. These expressions show that a given component ξ_j vanishes if one of two conditions is met; either the corresponding electric field component E_j is zero or it is in phase or π out of phase with the other two
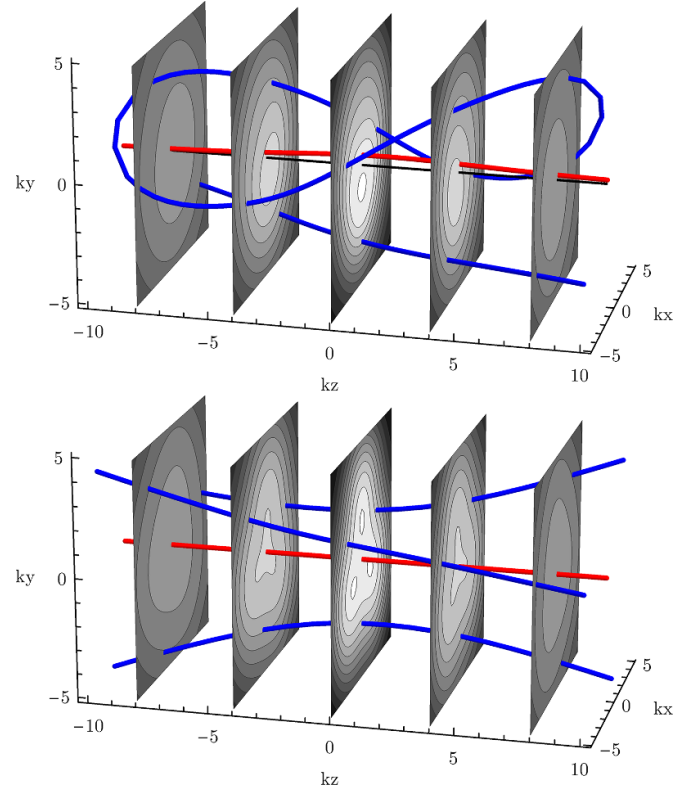
Figure 6. Argument of the components of $\boldsymbol{\xi}$ for the lemon (top) and star (bottom) FP fields with $k\zeta = 5$ and $\delta = \pi/4$, with L^T points marked by crosses. These plots use the same color palette as figure 4 for the phase.

components. The latter indicates the presence of an L^T point while the former is a special case which can be an L^T point if any of the other components of $\boldsymbol{\xi}$ vanish.

Figure 6 shows the argument of each component of $\boldsymbol{\xi}$ for the lemon and star FP fields presenting different possible behaviors. The points marked with a cross indicate the presence of an L^T point and they correspond to zeros for all three components of $\boldsymbol{\xi}$. These also correspond to the maxima of $|\psi|$ shown in figures 4 and 5. Other vortices that do not correspond to L^T points can be seen in figure 6; these are points where the corresponding component of the electric field is zero but the remaining two components are neither in phase nor π out of phase, as evidenced by the lack of vortices for the other components of $\boldsymbol{\xi}$ at that location. Note that both FP fields no longer have a line of linear polarization across the transverse plane but rather a set of three L^T points, which are equally distributed azimuthally for the star FP field but not for the lemon FP field.

3.4. True polarization lines

Upon propagation, the C^T and L^T points form lines that can either remain open or form closed loops. Figure 7 shows these trajectories, which have been found numerically, along with transverse cuts of the amplitude of the field. For the lemon FP field all the singularities rotate around the origin under propagation, and two of the L^T points merge to form an unknotted closed L^T loop, an unknot. This loop becomes smaller/larger for (more/less focused) fields with smaller/larger ζ. The C^T line near the z axis turns around it and approaches it asymptotically away from the focal region. For the star FP field, on the other hand, the singularities rotate around the origin but remain open since the threefold symmetry prevents any two of them from merging, and the central C^T line coincides exactly with the z axis. For both FP fields, the C^T points that are further from the origin spiral out away from the focal plane moving further into regions where the intensity is negligible (figures 4 and 5) and are thus not shown in figure 7. Note that L^T points always coincide with transverse L points (but
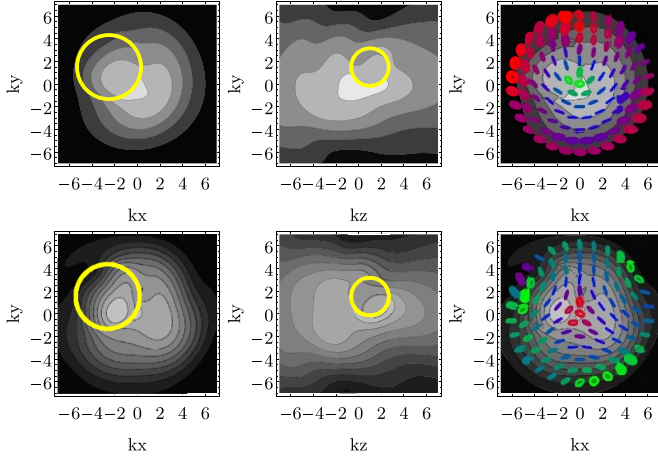

Figure 7. Trajectories of the L^T (blue) and C^T (red) points for the lemon (top) and star (bottom) FP fields with $k\zeta = 5$ and $\delta = \pi/4$.

not conversely), as opposed to C^T points. This confines L^T lines to the surfaces traced by the transverse L points. These L surfaces need to be topologically different from a cylinder in order to support knotted or linked L^T lines. However, for the FP fields studied here, the L surfaces are topologically equivalent to cylinders and can therefore support only open lines and unknots.
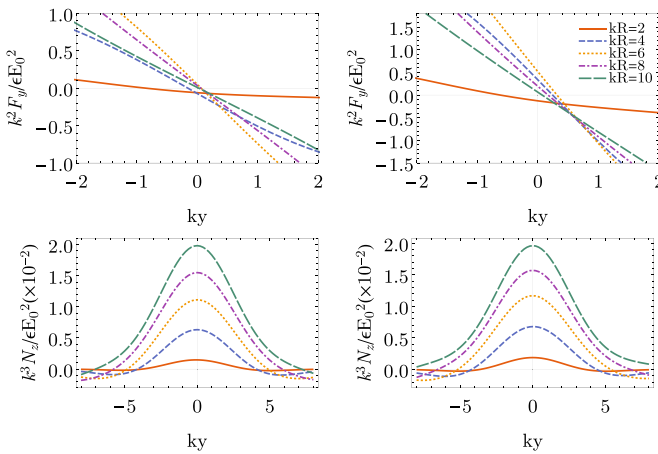
4. Mie scattering of FP fields

An advantage of the simple form of the FP fields defined here is that their multipolar decomposition can be computed analytically given any relative position between the focus of the multipolar basis and that of the FP fields. Therefore, the FP fields lend themselves to an analytic treatment of their scattering by a spherical particle, albeit with an infinite sum, from which the induced forces and torques can be computed [38, 52, 53] without recurring to Rayleigh's approximation [40, 54]. Figure 8 shows the total field after being scattered by a spherical particle of radius $kR = 3$ and refractive index $\nu_0 = 1.3 + 10^{-4}$i in free space, for both lemon and star FP fields. Note that the scattering changes significantly the intensity profile of the fields, but not the polarization distribution which is topologically stable. This can be appreciated in figure 8 where the polarization distribution is deformed but the lemon and star C points are still present.

Having solved the scattering problem, the forces and torques induced on the scatterer can be easily computed
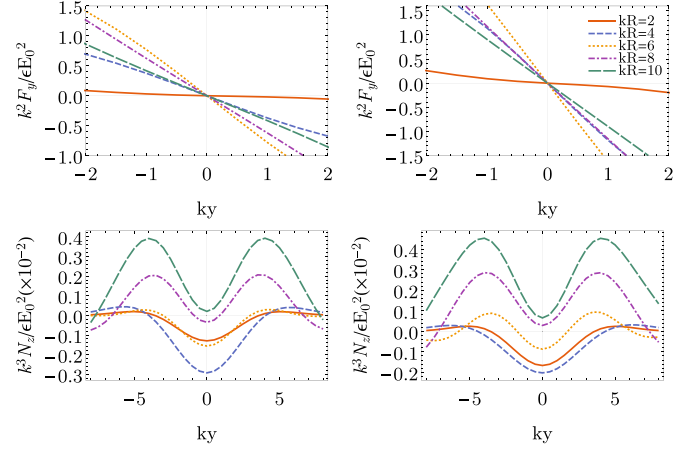
Figure 8. Amplitude distribution for the total field generated by the scattering of the lemon (top) and star (bottom) FP fields, with $k\zeta = 5$ and $\delta = \pi/4$, over the x–y plane (left) and the y–z plane (center), and the amplitude over the x–y plane with the transverse polarization distribution overlaid (right). The scattering particle is a sphere with refractive index $\nu_0 = 1.3 + 10^{-4}$i and radius $kR = 3$ located at $kr_p = (-2.5, 1.5, 1)$. The yellow circles show the transverse cut of the sphere by the corresponding plane.
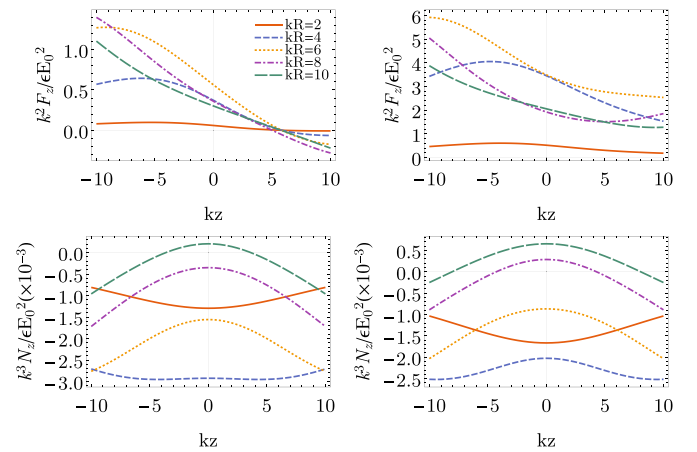

Figure 10. Variation of the y component of the force (top) and the z component of the torque (bottom) along the y axis, exerted by a star FP field ($k\zeta = 10$ and $\delta = \pi/4$) on a spherical particle with index of refraction $\nu_0 = 1.1 + 10^{-4}$i (left) and $\nu_0 = 1.3 + 10^{-4}$i (right) as a function of its radius R.

Figure 9. Variation of the y component of the force (top) and the z component of the torque (bottom) along the y axis, exerted by a lemon FP field ($k\zeta = 10$ and $\delta = \pi/4$) on a spherical particle with index of refraction $\nu_0 = 1.1 + 10^{-4}$i (left) and $\nu_0 = 1.3 + 10^{-4}$i (right) as a function of its radius R.

Figure 11. Variations of the z components of the force (top) and torque (bottom) along the z axis, exerted by a star FP field ($k\zeta = 10$ and $\delta = \pi/4$) on a spherical particle with index of refraction $\nu_0 = 1.1 + 10^{-4}$i (left) and $\nu_0 = 1.3 + 10^{-4}$i (right) as a function of its radius R.

[38, 55]. Figure 9 shows the variations of the y component of the force and the z component of the torque along the y axis for the lemon FP field. Due to the field's asymmetric intensity distribution, the zero point of lateral force is offset to $y < 0$ for smaller particles. However, surprisingly, for larger particles this zero force point is shifted to $y > 0$. Both shifts become more pronounced for particles with a higher real part of the refractive index. Another interesting feature is that the z component of the torque can take negative values at the edges of the focus even if the total angular momentum of the surrounding vortex field is zero due to its polarization opposite to the vortex charge.
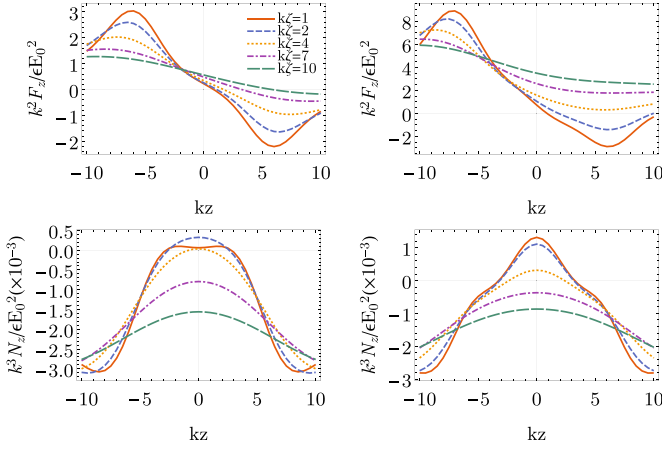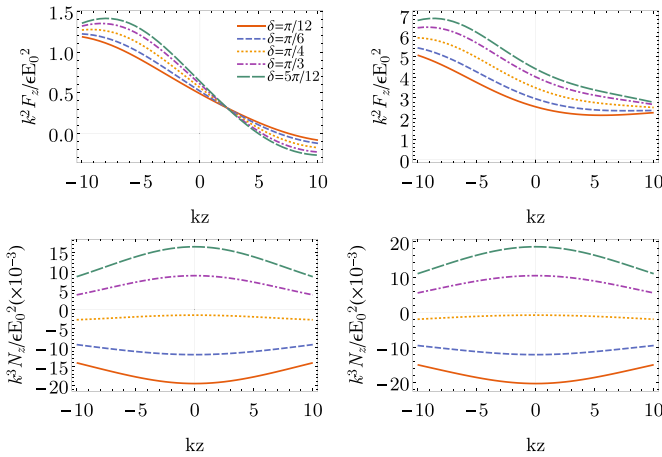
Given the symmetric shape of the star FP field, a point of zero transverse force is always located at $y = 0$ and is stable in this case, as shown in figure 10. This allows on-axis trapping if the particle properties are chosen correctly. Trapping in three directions is only possible if the z component of the force also presents a zero point along the z axis with negative slope. Figure 11 shows that, as a general rule, it is easier to trap smaller particles with a lower real index of refraction. The trapping location is located after the focus where the gradient force balances the radiation pressure. The presence and location of a stable point also depends on the degree of focusing: a field that is more focused produces a greater intensity gradient closer to the focal region thus increasing its trapping capabilities, as shown in figure 12. These observations are in line with intuition.

Figure 12. Variations of the z components of the force (top) and torque (second row) along the z axis, exerted by a star FP field with $\delta = \pi/4$ as a function of the degree of focusing ζ on a spherical particle of radius $kR = 6$ and index of refraction $\nu_0 = 1.1 + 10^{-4}i$ (left) and $\nu_0 = 1.3 + 10^{-4}i$ (right).

Figure 13. Variations of the z components of the force (top) and torque (second row) along the z axis, exerted by a star FP field with $k\zeta = 10$ as a function of the ratio δ on a spherical particle of radius $kR = 6$ and relative index of refraction $\nu_0 = 1.1 + 10^{-4}i$ (left) and $\nu_0 = 1.3 + 10^{-4}i$ (right).

The torque induced by the star FP field along the z axis has only a z component, which is highly dependent on the size of the particle (see figure 11): if the particle is small then it only interacts with the inner part of the field which mainly carries left-circularly polarized light generating a negative torque; on the other hand, if the particle is large then it is affected by the vortex in which the orbital and spin angular momentum couple constructively in the opposite sense than the angular momentum of the inner part of field. Therefore, the z component of the induced torque goes from being negative for smaller particles to being positive for larger particle. Alternatively, if the field is more focused then the region of left circular polarization shrinks, hence increasing the effect of the outer region on smaller particles. The behavior of the induced torque as the focusing properties are changed is shown in figure 12 where its sign changes as the field is more focused.

The parameter δ, controlling the ratio between the two orthogonal polarization components, can also be tuned to obtain a desired effect. As already mentioned, this parameter changes the spread of the polarization distribution without changing the level of focusing. This effect allows the control of the induced torque without affecting the trapping properties of the field, as shown in figure 13. It can then be used to twist the trapped particle by generating a torque that changes sign on each side of the trapping location.

5. Concluding remarks

In the paraxial regime FP beams are defined through the stereographic mapping of the PS onto the transverse plane. However, they can also be defined through a stereographic mapping from the PS onto the Fourier plane. This alternative view was exploited here to define nonparaxial FP fields through a mapping of the PS onto the SD, which is the nonparaxial extension of the Fourier plane for monochromatic fields. The mappings of polarization and amplitude were chosen so that the resulting fields ha analytic expressions in terms of vector multipoles evaluated at complex arguments. It was shown that the transverse polarization has the same generic structure as of the paraxial FP beams.

The true polarization singularities, obtained by taking into account the three-dimensional nature of polarization, were studied with the help of the auxiliary fields ψ and $\boldsymbol{\xi}$. The latter was used to aid in the identification of L^T points since it exhibits phase vortices in its components at L^T points, much like ψ facilitates finding C^T points. These true singularities trace lines across space that either remain open or form closed loops.

While the original FP beams were introduced as a way to map all paraxial polarization states onto the transverse plane, in the nonparaxial case it becomes impossible for a monochromatic field to span all possible three-dimensional polarization states. This is a simple consequence of the difference in dimensionality between the polarization and physical spaces; the former is a four-dimensional manifold (the product of two spheres [46, 47]) while the latter is the three-dimensional Euclidean space.

Several generalizations to this work are possible. One would be the extension of the sphere-to-sphere mapping to include higher order (radial and azimuthal) FP fields by increasing the number of cycles in the polar and azimuthal angles. This would involve replacing the spherical harmonics in equation (7) by higher-order ones, so that the field can still be expressed analytically in terms of multipoles [60]. Also, other polarization singularities could be considered, such as the monstar or other asymmetric structures [56, 57]. Finally, an interesting alternative would be to consider other forms of the function $f(\theta)$ introduced in equation (5) to generate the sphere-to-sphere mapping. One possibility is to use combinations of real exponentials, leading to sums of CF fields with different values of the parameter ζ, as in a type of basis function introduced recently [37, 58, 59].

Acknowledgment

ORCID iDs

Rodrigo Gutiérrez–Cuevas ⬤ https://orcid.org/0000-0002-3451-6684
Miguel A Alonso ⬤ https://orcid.org/0000-0001-7037-5383

References

[1] Rubinsztein-Dunlop H *et al* 2017 *J. Opt.* **19** 013001
[2] Gbur G J 2016 *Singular Optics* (Boca Raton: CRC Press)
[3] Rosales-Guzmán C, Ndagano B and Forbes A 2018 *J. Opt.* **20** 123001
[4] Bazhenov V Y, Vasnetsov M V and Soskin M S 1990 *JETP. Lett.* **52** 429
[5] Heckenberg N R, McDuff R, Smith C P and White A G 1992 *Opt. Lett.* **17** 221
[6] Beijersbergen M, Coerwinkel R, Kristensen M and Woerdman J 1994 *Opt. Commun.* **112** 321
[7] Arrizón V, Ruiz U, Carrada R and González L A 2007 *J. Opt. Soc. Am.* A **24** 3500
[8] Naidoo D, Roux F S, Dudley A, Litvin I, Piccirillo B, Marrucci L and Forbes A 2016 *Nat. Photon.* **10** 327
[9] Rubano A, Cardano F, Piccirillo B and Marrucci L 2019 *J. Opt. Soc. Am.* B **36** D70
[10] Maurer C, Jesacher A, FÃŒrhapter S, Bernet S and Ritsch-Marte M 2007 *New J. Phys.* **9** 78
[11] Levy U, Silberberg Y and Davidson N 2019 *Adv. Opt. Photonics* **11** 828
[12] Nieminen T A, Heckenberg N R and Rubinsztein-Dunlop H 2008 *Opt. Lett.* **33** 122
[13] Neves L, Lima G, Delgado A and Saavedra C 2009 *Phys. Rev.* A **80** 042322
[14] Forbes A and Nape I 2019 *AVS Quantum Sci.* **1** 011701
[15] Nye J F and Hajnal J V 1987 *Proc. R. Soc. Lond. A. Math. Phys. Sci.* **409** 21
[16] Berry M and Dennis M 2001 *Proc. R. Soc. Lond. Ser. A: Math. Phys. Eng. Sci.* **457** 141
[17] Dennis M 2002 *Opt. Commun.* **213** 201
[18] Dennis M R, O'Holleran K and Padgett M J 2009 *Progress in Optics* (Elsevier) pp 293–363
[19] Milione G, Sztul H I, Nolan D A and Alfano R R 2011 *Phys. Rev. Lett.* **107** 053601
[20] O'Holleran K, Dennis M R, Flossmann F and Padgett M J 2008 *Phys. Rev. Lett.* **100** 053902
[21] Flossmann F, O'Holleran K, Dennis M R and Padgett M J 2008 *Phys. Rev. Lett.* **100** 203902
[22] O'Holleran K, Dennis M R and Padgett M J 2009 *Phys. Rev. Lett.* **102** 143902
[23] Larocque H, Sugic D, Mortimer D, Taylor A J, Fickler R, Boyd R W, Dennis M R and Karimi E 2018 *Nat. Phys.* **14** 1079
[24] Sugic D and Dennis M R 2018 *J. Opt. Soc. Am.* A **35** 1987
[25] Freund I 2002 *Opt. Commun.* **201** 251
[26] Otte E, Alpmann C and Denz C 2016 *J. Opt.* **18** 074012
[27] Arora G 2019 Ruchi and P. Senthilkumaran *Opt. Lett.* **44** 5638
[28] Beckley A M, Brown T G and Alonso M A 2010 *Opt. Express* **18** 10777
[29] Beckley A M, Brown T G and Alonso M A 2012 *Opt. Express* **20** 9357
[30] Galvez E J, Khadka S, Schubert W H and Nomoto S 2012 *Appl. Opt.* **51** 2925
[31] Zhu W, Shvedov V, She W and Krolikowski W 2015 *Opt. Express* **23** 34029
[32] Yu P, Liu Y, Wang Z, Li Y and Gong L 2020 *Ann. Phys.* **532** 2000110
[33] Berry M V 1994 *J. Phys. A: Math. Gen.* **27** L391
[34] Sheppard C J R and Saghafi S 1998 *Phys. Rev.* A **57** 2971
[35] Moore N J and Alonso M A 2009a *J. Opt. Soc. Am.* A **26** 1754
[36] Moore N J and Alonso M A 2009b *J. Opt. Soc. Am.* A **26** 2211
[37] Gutiérrez–Cuevas R and Alonso M A 2017a *Opt. Express* **25** 14856
[38] Gutiérrez–Cuevas R, Moore N J and Alonso M A 2018 *Phys. Rev.* A **97** 053848
[39] Richards B and Wolf E 1959 *Proc. R. Soc. Lond.* A **253** 358
[40] Novotny L and Hecht B 2006 *Principles of Nano-Optics* (Cambridge: Cambridge University Press)
[41] Chen W, Chen Y and Liu W 2019 *Phys. Rev. Lett.* **122** 153907
[42] Kubo H and Nagata R 1983 *J. Opt. Soc. Am.* **73** 1719
[43] Jammalamadaka S R and Sengupta A 2001 *Topics in Circular Statistics* vol 5 (London: World Scientific Publishing)
[44] Gutiérrez–Cuevas R and Pisanty E 2020 Complexfocus GitHub allowbreak4299909
[45] Bliokh K Y, Alonso M A, Ostrovskaya E A and Aiello A 2010 *Phys. Rev.* A **82** 063825
[46] Hannay J H 1998 *J. Mod. Opt.* **45** 1001
[47] Bliokh K Y, Alonso M A and Dennis M R 2019 *Rep. Prog. Phys.* **82** 122401
[48] Phillips C L, Peterka T, Karpeyev D and Glatz A 2015 *Phys. Rev.* E **91** 023311
[49] Taylor A J and Dennis M R 2016 *Nat. Commun.* **7** 12346
[50] Freund I 2001 *Opt. Lett.* **26** 1996
[51] Freund I, Mokhun A I, Soskin M S, Angelsky O V and Mokhun I I 2002 *Opt. Lett.* **27** 545
[52] Moore N J and Alonso M A 2008 *Opt. Express* **16** 5926
[53] Moore N J and Alonso M A 2016 *J. Opt. Soc. Am.* A **33** 1236
[54] Wang L-G 2012 *Opt. Express* **20** 20814
[55] Barton J P, Alexander D R and Schaub S A 1989 *J. Appl. Phys.* **66** 4594
[56] Kumar V, Philip G M and Viswanathan N K 2013 *J. Opt.* **15** 044027
[57] Galvez E J, Rojec B L, Kumar V and Viswanathan N K 2014 *Phys. Rev.* A **89** 031801
[58] Gutiérrez–Cuevas R and Alonso M A 2017b *Opt. Lett.* **42** 2205
[59] Gutiérrez–Cuevas R and Alonso M A 2017c *J. Opt. Soc. Am.* A **34** 1697
[60] Gutiérrez-Cuevas R and Pisanty E. Optical polarization skyrmionic fields in free space *J. Opt.* (https://doi.org/10.1088/2040-8986/abe8b2)